

Intelligent Anomaly Detection for Lane Rendering Using Transformer with Self-Supervised Pre-Training and Customized Fine-Tuning

Yongqi Dong^{#,*}

Faculty of Civil Engineering and Geosciences
Delft University of Technology, Delft, The Netherlands, 2628 CN
Email: yongqi.dong@rwth-aachen.de

Xingmin Lu[#]

School of Electrical and Control Engineering
North China University of Technology, Beijing, China, 100144
Email: lxm.xupt@gmail.com

Ruohan Li

Department of Civil and Environmental Engineering, College of Engineering
Villanova University, Villanova, USA, PA 19085
Email: rli04@villanova.edu

Wei Song^{*}

School of Information Science and Technology
North China University of Technology, Beijing, China, 100144
Email: songwei@ncut.edu.cn

Bart van Arem

Faculty of Civil Engineering and Geosciences
Delft University of Technology, Delft, The Netherlands, 2628 CN
Email: b.vanArem@tudelft.nl

Haneen Farah

Faculty of Civil Engineering and Geosciences
Delft University of Technology, Delft, The Netherlands, 2628 CN
Email: h.farah@tudelft.nl

[#] These authors contributed equally to this work and should be considered as co-first authors.

^{*} Corresponding authors: Yongqi Dong (yongqi.dong@rwth-aachen.de) and Wei Song (songwei@ncut.edu.cn).

Submitted [27 November, 2024]

ABSTRACT

The burgeoning navigation services using digital maps provide great convenience to drivers. Nevertheless, the presence of anomalies in lane rendering map images occasionally introduces potential hazards, as such anomalies can be misleading to human drivers and consequently contribute to unsafe driving conditions. In response to this concern and to accurately and effectively detect the anomalies, this paper transforms lane rendering image anomaly detection into a classification problem and proposes a four-phase pipeline consisting of data pre-processing, self-supervised pre-training with the masked image modeling (MiM) method, customized fine-tuning using cross-entropy based loss with label smoothing, and post-processing to tackle it leveraging state-of-the-art deep learning techniques, especially those involving Transformer models. Various experiments verify the effectiveness of the proposed pipeline. Results indicate that the proposed pipeline exhibits superior performance in lane rendering image anomaly detection, and notably, the self-supervised pre-training with MiM can greatly enhance the detection accuracy while significantly reducing the total training time. For instance, employing the Swin Transformer with Uniform Masking as self-supervised pretraining (Swin-Trans-UM) yielded a higher accuracy of 94.77% and an improved Area Under The Curve (AUC) score of 0.9743 compared with the pure Swin Transformer without pre-training (Swin-Trans) with an accuracy of 94.01% and an AUC of 0.9498. Furthermore, the fine-tuning epochs were dramatically reduced to 41 from the original 280. Ablation study regarding techniques to alleviate the data imbalance between normal and abnormal instances further reinforces the model's overall performance, with the 2-class classification variant of the Swin-Trans-UM model, i.e., Swin-Trans-UM_2 obtained the best performance on all the evaluation metrics. In conclusion, the proposed pipeline, with its incorporation of self-supervised pre-training using MiM and other advanced deep learning techniques, emerges as a robust solution for enhancing the accuracy and efficiency of lane rendering image anomaly detection in digital navigation systems.

Keywords: Anomaly Detection, Lane rendering image, Transformer, Masked image modeling, Self-supervised learning, Image classification

INTRODUCTION

With the increase of private car ownership and the emergence of information and communication technology (ICT), navigation services become popular, gaining increasing importance, forming a crucial component in driving, and providing convenience for drivers. Navigation services are always backed up by digital map applications (1, 2). A critical aspect of digital maps is the background, which is generated through data rendering. However, lane-level rendered map images may contain anomalies (errors and/or defects), such as irregular shapes and missing edges or corners. Examples of anomalies are illustrated in **Figure 1**. These anomalies can be confusing for human drivers, impairing their understanding and decision-making during navigation, which might result in critical unsafe situations.

Similar anomalies can occur in high-definition (HD) maps used by automated vehicles (AVs) (3, 4). Accurate lane rendering in such maps is essential for various systems, including automated driving systems, Advanced Driver-Assistance Systems (ADAS), and smart traffic management systems, all of which rely heavily on precise and reliable mapping data to function effectively and safely. Anomalies in such maps can lead AVs into unsafe regions or induce dangerous driving behaviors.

Furthermore, this targeted problem is closely related to and can be easily transformed into relevant critical and practical real-world applications, such as road anomaly detection (5, 6), road defect detection (7, 8), as well as anomaly detection for lane and pavement marking on roads (9–11). These issues are even more crucial for road safety; thus for example, the Federal Highway Administration (FHWA) in the USA, has detailed guidelines on pavement markings essential for safe navigation and traffic management (12). Similarly, China's Ministry of Transport emphasizes the importance of accurate lane marking for reducing accidents and enhancing road safety (13).

Overall, it is vital to correctly detect these anomalies to prevent such unsafe situations. Fortunately, with the advancement of artificial intelligence algorithms, particularly in the domain of computer vision, it is now possible to carry out intelligent and automatic anomaly detection.

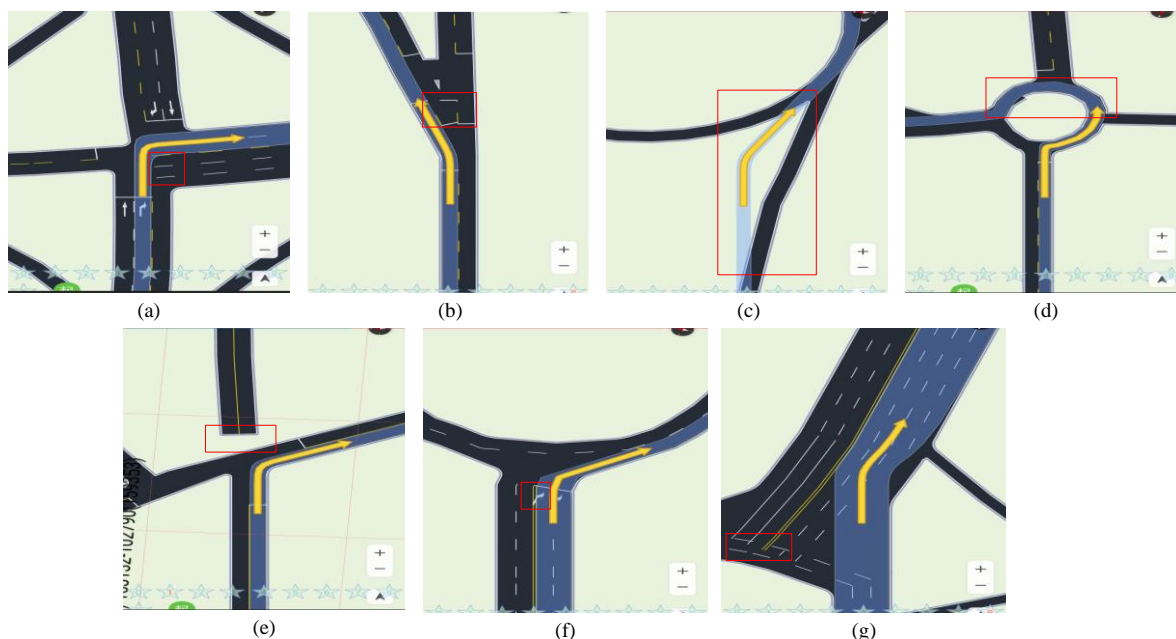


Figure 1 Illustration for examples of anomalous lane rendering images

Anomaly types notes: (a) Anomaly_1: The road center line extends out of the junction; (b) Anomaly_2: The stop line is in the middle of a road; (c) Anomaly_3: The navigation route does not match actual roads; (d) Anomaly_4: The road shoulder is bumpy; (e) Anomaly_5: A part of the road is missing; (f) Anomaly_6: The road marking arrows overlap; (g) Anomaly_7: The lane lines overlap. The red boxes mark the specific regions where the anomalies are.

Conventional studies regarding anomaly detection in the relevant transportation domains principally focus on road surface anomalies (5, 14), road traffic anomalies (15, 16), in-vehicle and vehicle-to-vehicle communication anomalies (17, 18), abnormal driving behaviors (19–21), etc. Multi-modal and multi-source data have been utilized with various machine learning methods to do the detection. However, few studies have employed self-supervised methods to leverage unlabeled data. On the other hand, masked autoencoders and, to be general, masked image modeling (MiM) have become popular pre-training paradigms for self-supervised visual representation learning tasks. In MiM, a portion (usually a high ratio of 50% or above) of the input image is randomly masked using patches, and the model tries to reconstruct the masked pixels according to the target representations. The pre-trained model weights through MiM can be transferred to the downstream task for fine-tuning. Evidence in recent studies, e.g., (22–26), has demonstrated that self-supervised pre-training with MiM can boost the downstream tasks (e.g., classification, segmentation, and object detection) to achieve better desirable performance. Thus it is worth exploring MiM-based pre-training for anomaly detection.

Furthermore, although various image datasets (e.g., animals, digital numbers, industrial inspection image MVTEC AD datasets (27)) and vision-based anomaly detection methods have been developed (28–32), to the best of the authors and after extensive review, there are no studies that tackle the abnormal lane rendering images in digital navigation maps.

To fill the aforementioned research gaps, this study develops a four-phase pipeline with self-supervised pre-training and customized fine-tuning and using state-of-the-art Transformer models (22, 33–37) to accurately and effectively detect lane rendering image anomalies. A large-scale lane rendering image dataset adjusted from the [2022 Global AI Challenge](#) with both labeled and unlabeled data was adopted and extensive experiments were carried out tackling the lane rendering image anomaly detection problem as a 2-class, 8-class, or 9-class classification task. Results verify the proposed pipeline with the best model delivering performance at an accuracy of 94.82%, the Area Under the Curve (AUC) at 0.9756, and the F1-measure at 0.7879. To summarize, the main contributions of this paper lie in:

1. Transforming the lane rendering anomaly detection problem into a 2-class, 8-class, or 9-class classification problem;
2. Proposing a four-phase pipeline with especially self-supervised pre-training and customized fine-tuning to tackle the lane rendering image anomaly detection problem;
3. Customizing and implementing two MiM self-supervised pre-training methods using state-of-the-art Transformer models within the proposed four-phase pipeline and carrying out extensive training, fine-tuning, and validating experiments;
4. Delivering excellent detection performance in terms of various evaluation metrics.

Please note the methods and models developed in this study can not only effectively detect lane rendering image anomalies but also can be readily adapted for related applications, such as detecting road surface anomalies and identifying abnormal lane markings.

The rest of this paper is arranged as follows: The next section describes the research methodology consisting of the proposed pipeline in detail including the overall framework, data pre-processing, self-supervised pre-training, customized fine-tuning, and post-processing; Following this, Section *EXPERIMENT AND RESULTS* shows the experimental set-up and results comparing different models within the proposed pipeline, the results and discussion. Then, the *ABLATION STUDY* section introduces methods to alleviate data imbalance. Finally, section *CONCLUSIONS, LIMITATIONS, AND FUTURE RESEARCH* draws the findings, lists the limitations, and proposes insights for future studies.

METHODOLOGY

In this section, the proposed method is introduced in detail. Firstly, the overall architecture of the proposed four-phase pipeline is illustrated and briefly explained. Then, each of the four phases, i.e., image pre-processing, self-supervised pre-training, fine-tuning classification, and post-processing, is depicted with comprehensive delineations sequentially.

A. Overall pipeline description

This study proposes a pipeline of four phases to tackle the anomaly detection task for lane rendering images in digital navigation APPs. The overall pipeline of the four-phase method is illustrated in **Figure 2**.

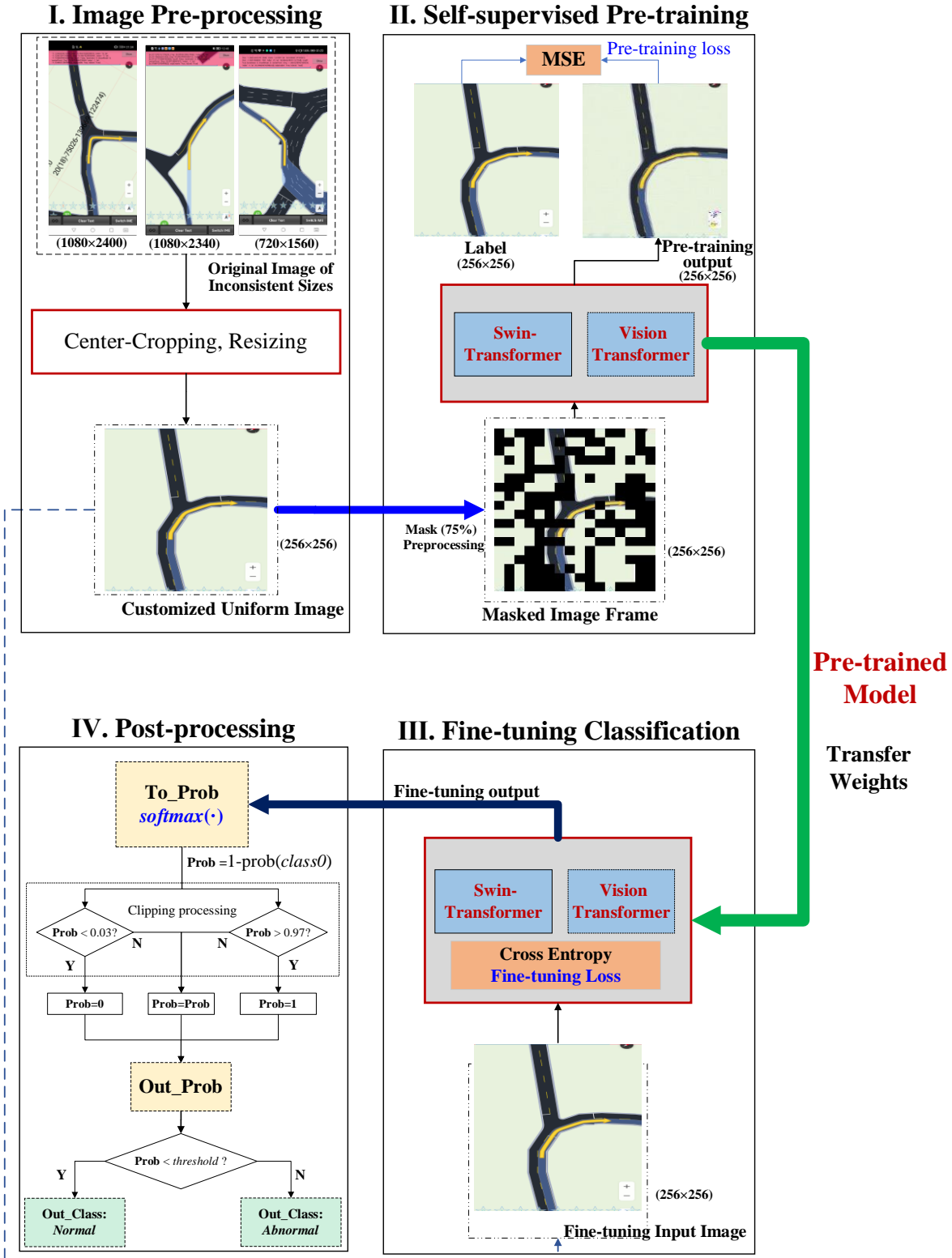


Figure 2 The architecture of the proposed four-phase pipeline

Note: class 0 is the normal class.

The designed 4 phases are **1)** Image pre-processing, which normalizes the inconsistent images into uniform format, size, and resolution; **2)** self-supervised pre-training, which is tackled by the masked image modeling (MiM) method using mean square error (MSE) loss and outputs the pre-trained model; **3)** customized fine-tuning, which adopts the pre-trained model weights and further fine-tune the neural network model as a classification task using cross-entropy based loss (or its variants) with label smoothing; and **4)** post-processing, which transforms the results of the last neural network layer (i.e., the output layer) into classification probabilities and outputs the final detection results with tuned probability threshold. The following subsections explain these four phases in more detail.

B. Image pre-processing

This study adopts the large-scale lane rendering image dataset adjusted and rearranged from the [2022 Global AI Challenge](#). The provided original images get different resolutions and sizes. The majority of them have a resolution of 1080 * 2400, while there are a few images with different resolutions, i.e., 1080 * 2340 and 720 * 1560. Furthermore, to focus on the relevant content of the images, the study identifies that the top and bottom portions contain non-map-related regions. Therefore, this study first carried out a center-cropping operation by removing the 1080 * 300 pixels at the top and 1080 * 240 pixels at the bottom of the images, and then scaled the images to the same resolution of 256 * 256. Furthermore, since the images are only partly labeled with ground truth (i.e., class label of normal or anomaly type), while a large proportion of the images are unlabeled, this study constructs a pre-training dataset with both labeled images and unlabeled images, a fine-tuning dataset with partly random selected labeled image, and a testing dataset with a small proportion of the labeled images which is unseen in the fine-tuning dataset.

Similar image datasets can be created for other navigation maps by taking screenshots of the application software interface and applying the aforementioned pre-processing steps. The same process can be applied to real-world image datasets collected by cameras for anomaly detection of e.g., road lane line markings or pavement markings. It is important that after the image pre-processing phase, the images are in the uniform format, size, and resolution.

C. Self-supervised pre-training

For the lane rendering images in the navigation map APPs, lane lines account for only a small fraction of the whole image as shown in **Figure 1**. There are 7 types of anomalies in the studied dataset, while the majority of the lane rendering images are normal ones. With these circumstances, it is assumed there is more spatial redundancy regarding image features for the abnormal lane rendering image detection task and thus stronger feature extraction ability is required. Therefore, it is necessary to design a method to fully extract aggregated context information, as well as the critical features and correlations among pixels. Furthermore, as the examined dataset consists of massive unlabeled images (more than 80%), it is also vital to settle a pipeline to make full use of these unlabeled images.

Motivated by the aforementioned, this study proposes and customizes the MiM method for self-supervised pre-training. In this phase, the total set of images serves as inputs for model pre-training regardless of whether labeled or unlabeled. The input image is randomly masked using patches, and the pre-training model tries to reconstruct the masked pixels to match the target original images. Generally, the standard objective of self-supervised pre-training with MiM can be mathematically represented by **Equation 1**:

$$\min \frac{1}{\Omega(i_M)} \|\mathbf{r}_M - \mathbf{i}_M\|_2 \quad (1)$$

where $\mathbf{i}, \mathbf{r} \in \mathbb{R}^{3 \times H \times W}$ are the input original RGB values and the reconstructed RGB values, respectively (H is the height of the image, W is the width of the image, with $H \times W = 256 \times 256$ in this study); M represents the set of masked image pixels; $\Omega(\cdot)$ is the cardinality operator function to get the number of elements; $\|\cdot\|_2$ stands for ℓ_2 -norm. Accordingly, the objective involves minimizing the Root Mean Squared Error (RMSE), ℓ_2 loss, between the original and reconstructed pixel values for the masked regions. By focusing on accurately reconstructing the masked regions, the MiM approach encourages the model to learn rich and context-aware representations of the input image, which are crucial for downstream tasks.

Generally, there are two styles of implementing MiM: (1) raw pixel value regression, where the model directly reconstructs pixel values, and (2) converting the masked pixel signals into clusters or classes through methods such as vision tokenization (22, 38) or color clustering (39), followed by performing a classification task for masked image prediction. Accordingly, this paper customizes and implements two distinct MiM methods, i.e., Uniform Masking (36) and the method introduced in Bidirectional Encoder representation from Image Transformers (BEiT) (22). The Uniform Masking method was selected because it successfully enables efficient asymmetric structure, likewise in (24), of pixel-based Masked Autoencoder (MAE) style self-supervised pre-training, particularly for Pyramid-based Vision Transformers (ViTs). On the other hand, BEiT was selected because it serves as a typical and well-established representation of token-based methods. BEiT is the first to successfully adapt Masked Language Modeling (MLM) techniques from the Natural Language Processing (NLP) domain to the computer vision domain using ViT models. By introducing a discrete tokenization mechanism for MiM, BEiT enables ViTs to process images in a manner analogous to how Transformers handle textual data, marking a significant milestone in bridging the gap between NLP and computer vision tasks.

Regarding the Uniform Masking method, two key operations play a central role in the self-supervised learning process:

- 1) **Uniform Sampling:** This step ensures that one random patch is sampled from each $2 * 2$ grid of patches within the image. As a result, 75% of the targeted region is dropped, which enforces a uniform yet sparse sampling pattern across the image.
- 2) **Secondary Masking:** Since using only the uniform sampling can potentially make the self-supervisory task less challenging and largely hinders the representation quality (24), after uniform sampling, an additional random masking operation (termed *Secondary Masking*) is applied to the sampled regions, further masking 25% of them (as used in this study) as shared learnable tokens.

Integrating uniform sampling and secondary masking together enables the pre-training method to support Pyramid-based ViTs, e.g., (34, 40), while preserving better transferable visual representations. The Uniform Masking method pipeline for self-supervised learning is illustrated in **Figure 3**. The image is firstly divided into $16 * 16$ patches for *Uniform Sampling*, which drops up 75% of the original image, and the *Secondary Masking* is operated on the remaining patches. A compact 2D input, reduced to a quarter of the original image size, is constructed using the uniform-sampled patches combined with the secondary-masked tokens and is subsequently fed to the encoder. For the Pyramid-based ViT encoder, this study employs the Swin Transformer (34), which leverages a hierarchical architecture to effectively capture both local and global features, ensuring robust feature representation. For the decoder, the lightweight MAE Decoder, based on Vanilla ViT, is utilized, as adopted in (24). The MAE Decoder reconstructs the image using the encoder output features into the original size. These combinations ensure an efficient and effective architecture for self-supervised learning.

The selection of the masked ratio at 75% in the uniform sampling process is based on the experiment results reported in (24, 36), while the selection of the secondary masking ratio of 25% is based on the ablation experiment results reported in (36).

Regarding the BEiT self-supervised MiM method in (41), each image is pre-trained with two complementary views, i.e., image patches (e.g., $16 * 16$ pixels) and visual tokens (i.e., discrete tokens). **Figure 4** illustrates the method pipeline of BEiT for self-supervised MiM learning. The images are first "tokenized" into discrete visual tokens, which correspond to indices within a learned visual vocabulary. In this study, the visual vocabulary is generated using a discrete variational autoencoder (dVAE) tokenizer as in (22, 38). Following tokenization, some image patches are randomly masked and replaced with a special mask embedding before being fed into the ViT backbone encoder. Then, the objective of the self-supervised MiM pretraining task involves predicting the visual tokens of the original image from the encoded representations of the corrupted image, which effectively enables the model to learn robust visual features. The prediction of the visual tokens is handled by the MiM head which consists of a single linear layer that converts the encoded features from the ViT encoder into a format compatible with the visual

token space. Since the task involves finding the correct classes (i.e., the visual token indices), the Cross-Entropy loss function is employed for optimization. To reconstruct the full image, the dVAE decoder takes the predicted discrete tokens as input and reconstructs their corresponding image patches. It is important to note that the MiM head is only used during the pre-training phase; during fine-tuning, task-specific decoders replace the MiM head. In this study, the original fine-tuned hyperparameters and network architecture from (41) are adopted.

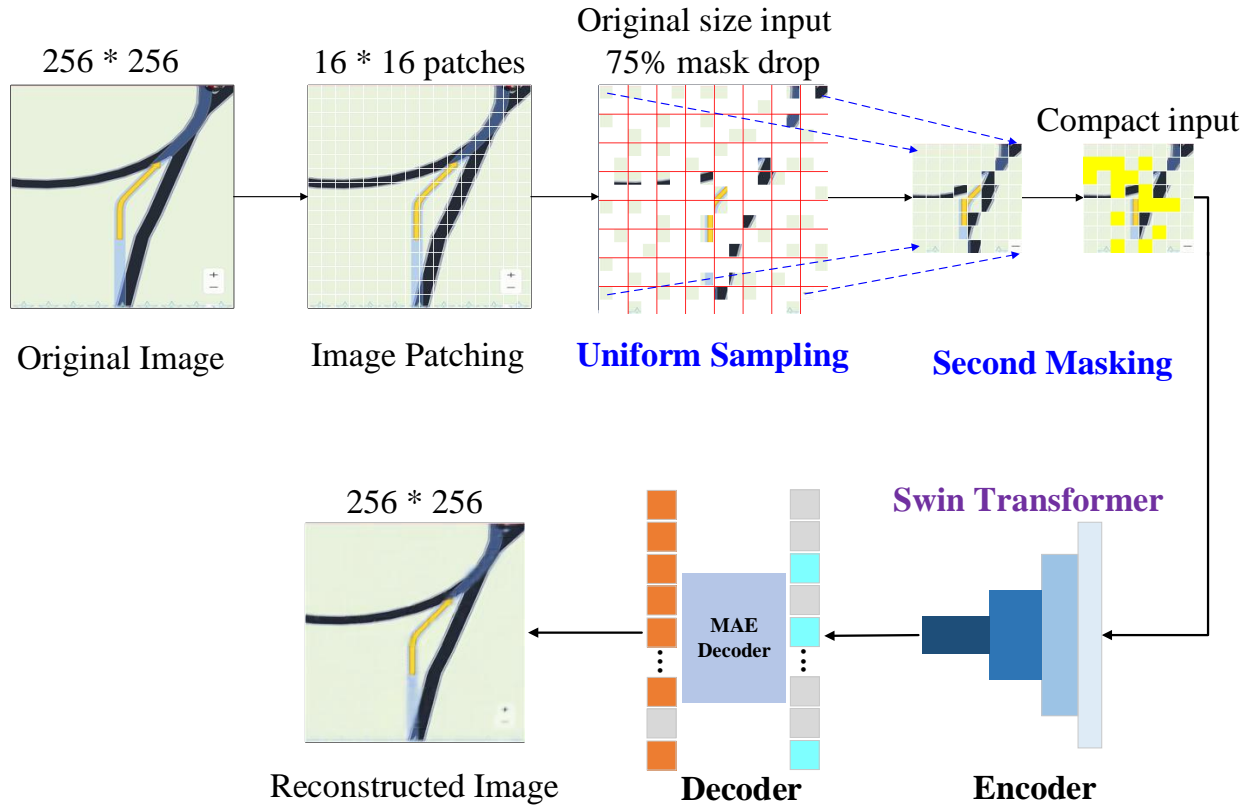


Figure 3 The illustration of the Uniform Masking method pipeline for MiM

The described MiM task, implemented through either the Uniform Masking method or the BEiT method, forces the model to learn meaningful representations of images by understanding the context of the unmasked patches. For the Uniform Masking method, the Swin Transformer encoder is pre-trained using masked image regions, encouraging the model to effectively capture spatial relationships and hierarchical features. During the downstream classification task, the weights of the pre-trained Swin Transformer encoder are retained, and the MAE Decoder is replaced by a classification decoder. In contrast, for the BEiT method, the ViT encoder is pre-trained to predict discrete visual tokens corresponding to masked image regions. This approach emphasizes token-based representations that align with concepts in the visual vocabulary. For the classification task, the pre-trained weights of the ViT encoder are preserved, and the MiM head is substituted with a task-specific classification decoder. Both methods leverage the robust features learned during the MiM task to enhance performance in the downstream tasks (i.e., the classification task of image types in this study), effectively transferring knowledge from the self-supervised pre-training phase to supervised fine-tuning.

This study also implemented and trained a Vision Transformer (ViT) model without the proposed self-supervised pretraining as a baseline.

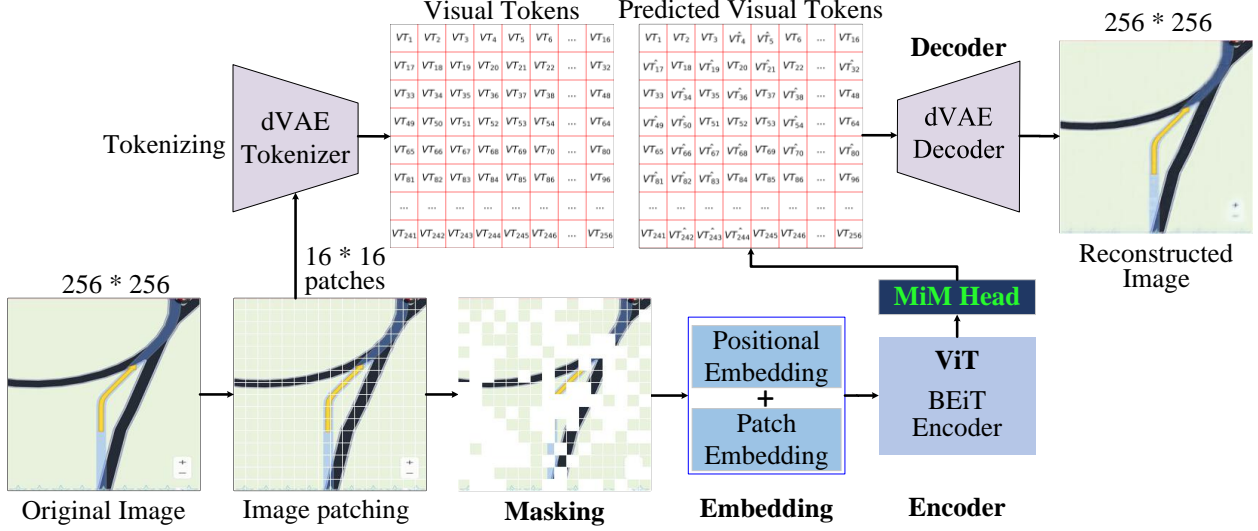


Figure 4 The illustration of the BEiT method pipeline for MiM

D. Customized fine-tuning

In this paper, the lane rendering images anomaly detection task is transferred into a 2-class, 8-class, or 9-class (multi-label) classification problem, with separating the 7 types of anomalies from the normal ones as the objective. The pre-training model weights in the self-supervised pre-training phase are transferred and further updated using the back-propagation mechanism with label smoothing Cross-Entropy as the loss function. To further boost the model performance, the mixed-up technique (42) is adopted.

E. Post-processing

After customized fine-tuning, during the testing stage, the fine-tuned model will be applied to assign "new" testing images that are unseen in the training process into the normal class or abnormal class. A post-processing phase is designed to aggregate the probability results and output the detection classification results.

In the post-processing, the neural network model outputs are first transformed into probabilities using $\text{softmax}(\cdot)$ function; and then the probability of each image being abnormal is calculated and truncated/clipped with up and down thresholds. After getting the truncated probability, the final detection result can be determined by fine-tuning a probability threshold to distinguish the anomalies and the normal image samples.

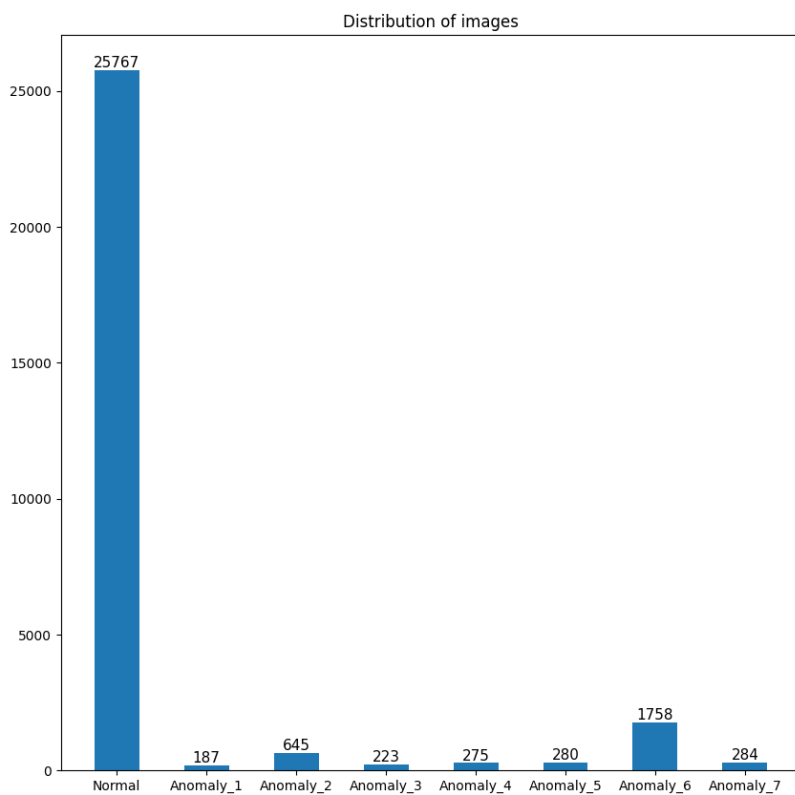
EXPERIMENT AND RESULTS

To verify the effectiveness of the proposed pipeline, extensive experiments were carried out under various settings.

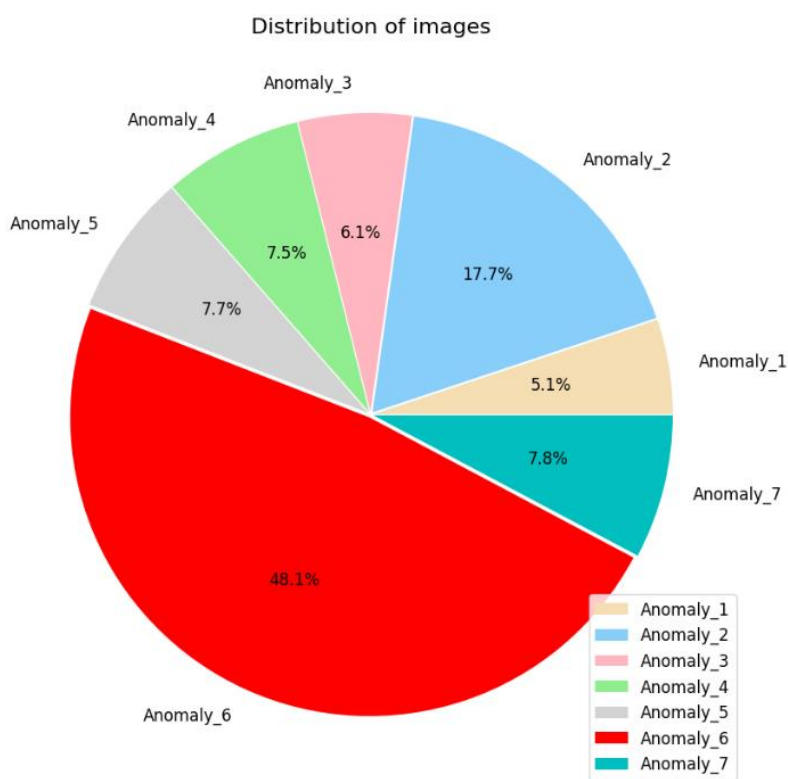
A. Data set description

The lane-rendering digital map image data used in this study are adjusted and rearranged from the [2022 Global AI Challenge](#). As aforementioned, there are 7 types of anomalies, e.g., Anomaly_1: The road center line extends out of the junction; Anomaly_2: The stop line is in the middle of a road; Anomaly_3: The navigation route does not match actual roads; Anomaly_4: The road shoulder is bumpy; Anomaly_5: A part of the road is missing; Anomaly_6: The road marking arrows overlap; Anomaly_7: The lane lines overlap. Examples are shown in **Figure 1**.

In total, there are 161,772 images with only 29,164 images labeled with the ground truth. Within the labeled ones, there are a total of 25,767 normal images and 3,397 images containing different kinds of abnormalities (please note some images exhibit multiple different types of anomalies). **Figure 5 (a)** shows the histogram plot for the distribution of all labeled images, while **Figure 5 (b)** illustrates the pie chart for



(a)



(b)

Figure 5 The distribution of labeled images: (a) histogram plot for the distribution of all labeled images and (b) pie chart for the distribution of each anomaly type within the labeled abnormal images

the distribution of each anomaly type within the labeled abnormal images. It is visible and clearly observed that within the 29,164 labeled images, the majority are normal ones. Furthermore, as illustrated in **Figure 5**, certain types of anomalies (e.g., Anomaly_6 and Anomaly_2) account for more samples than the other types of anomalies. Typically, Anomaly_6 takes up nearly half (48.1%) of the total quantity of abnormal images.

The labeled dataset is then randomly split into the training set, validation set, and test set, according to the ratio of 70%, 15%, and 15%, respectively. The images were classified according to error types, and images with multiple error types were put into multiple categories. Thus, it is a multi-class multi-label classification problem and there are a few more training examples than the image quantity. To be specific, in practice, the number of instances in the training set is 20,764, the number of instances in the validation set is 4,310, and the number of instances in the test set is 4,346. However, all the available 161,772 images regardless of whether labeled or not are adopted in the self-supervised pre-training process.

B. Tested Transformer models

Two Transformer models, i.e., Vision Transformer (ViT) (37) and Swin Transformer (34) are implemented and tested in this study. The two Transformer models are tested in modes of both with and without the self-supervised pre-training. Therefore, there are in total four model variants, i.e., 1) pure ViT without pretraining, 2) ViT variant, BEiT, with the pretraining method described in (22), 3) pure Swin Transformer (Swin-Trans for short), and Swin Transformer with the Uniform Masking as self-supervised pre-training method (Swin-Trans-UM for short). The detailed model architectures, i.e., parameter settings for each layer of the tested models, are illustrated in Appendix Table A1-A4.

C. Evaluation metrics

Various metrics are used to evaluate the overall performance of the selected models. Four basic terms, i.e., True-positive (TP) which represents the number of correctly detected lane rendering image anomalies, True-negative (TN) which represents the number of correctly detected normal lane rendering images, False-positive (FP) which represents the number of incorrectly detected anomalies, and False-negative (FN) which represents the number of incorrectly detected normal lane rendering images, are first obtained. Then, based on the four basic metrics, accuracy, precision, and recall were calculated.

Accuracy is the percentage of correctly predicted lane rendering image samples in regard to the total sample size, which can be defined as the following equation:

$$\text{Accuracy} = \frac{\text{TP} + \text{TN}}{\text{TP} + \text{TN} + \text{FP} + \text{FN}} \quad (2)$$

Precision is the number of correctly predicted positive lane rendering image anomalies as a percentage of the total number of predicted positive anomaly observations and it shows how close the measurements are to each other. The mathematical expression of precision is defined by

$$\text{Precision} = \frac{\text{TP}}{\text{TP} + \text{FP}} \quad (3)$$

Recall ratio is the percentage of positive anomaly observations correctly predicted in the actual category.

$$\text{Recall} = \frac{\text{TP}}{\text{TP} + \text{FN}} \quad (4)$$

Finally, the F1-score (F1 for short) provides an overall view of recall and precision (weighted average). F1 ranges from 0.0 to 1.0, with 1.0 indicating perfect precision and recall. And F1 can be obtained using the following equation:

$$F1 = 2 \times \frac{\text{Precision} \times \text{Recall}}{\text{Precision} + \text{Recall}} \quad (5)$$

Another appropriate indicator for evaluating the two-class classification problem is the Receiver Operating Characteristic-Area Under the Curve (ROC AUC), commonly abbreviated as AUC. AUC assesses the model's ability to distinguish between normal and anomalous instances. It provides a single scalar value summarizing the trade-off between the True Positive Rate (TPR) and the False Positive Rate (FPR) across different thresholds, offering insights into the model's classification performance regardless of the specific threshold applied. Given its threshold-independent nature and its ability to encapsulate the model's discriminative power, AUC is particularly suitable for imbalanced classification problems, such as the lane rendering image anomaly detection studied in this paper. Accordingly, this study selects AUC as the primary evaluation metric for comparing and assessing the performance of the tested models.

To measure AUC, one needs the TPR, i.e., recall ratio, and the FPR. TPR and TNR can be obtained by the following two equations

$$TPR = \frac{TP}{TP+FN} \quad (6)$$

$$FPR = \frac{FP}{TN+FP} \quad (7)$$

D. Experiment set-up

Configuration Details: In this paper, to reduce the computational payload and save training time, the size of the images for both the training set and test set is set to a resolution of 256×256. In pre-training, the proportion of masked patches is set to 75%. Experiments were carried out on four NVIDIA Tesla V100 (32 GB memory) GPUs, using PyTorch version 1.9.0 with CUDA Deep Neural Network library (cuDNN) version 11.1. The batch size is set to be as large as possible, which is 60. The learning rate was initially set to 0.001 with decay applied after each epoch.

Data Augmentation:

A data augmentation technique, MixUp (42), where two samples (inputs and their labels) are linearly combined is adopted to upgrade the model performance. The idea of MixUp is to create new synthetic samples to encourage the model to make predictions based on more diverse data.

The new synthetic training sample is given by the:

$$\tilde{x} = \lambda x_a + (1 - \lambda)x_b, \tilde{y} = \lambda y_a + (1 - \lambda)y_b \quad (8)$$

where x_a, x_b are two raw input sample vectors, y_a, y_b are the corresponding one-hot encoded labels, λ is the MixUP parameter.

The MixUp technique helps the model generalize better by exposing it to more interpolated data points leading to smoother decision boundaries.

Loss Function Details: As mentioned before, to make the proposed 4-phase pipeline work, different loss functions are adopted accordingly in the pre-training and fine-tuning phases. In the pre-training phase, the mean square error (MSE) is selected as the loss function for the Uniform Masking method since its objective is to reconstruct the masked patches directly at the pixel level. While the Cross-Entropy loss function is employed for BEiT method since its MiM task involves identifying the correct visual token indices, framing the problem as a classification task over a visual vocabulary.

In the fine-tuning phase, the objective is to classify the lane rendering images into normal ones and anomalies, which can be regarded as a typical classification task. The Cross-Entropy loss with label smoothing is adopted for this imbalanced classification task, which is illustrated in **Equation 9**:

$$\ell_{CE} = \ell(y, \hat{y}) = -(1 - \varepsilon) \log(\hat{y}_y) - \frac{\varepsilon}{c-1} \sum_{c \neq y} \log(\hat{y}_c) \quad (9)$$

where C is the number of classes; y is one-hot encoded true label; \hat{y} is the predicted probabilities output by the model, for example, \hat{y}_y is the predicted probability for the true class, and \hat{y}_c is the predicted probability for the true class c ; ε is the smoothing factor controlling the amount of uncertainty applied, usually set between 0 and 1.

With label smoothing, the true labels are adjusted to distribute some of the target probability mass to other classes. The overall effect of this modification is to provide a softer target. The model is less confident solely on one class, promoting better learning from non-ideal scenarios, such as label noise or ambiguity, and potentially improving generalization.

Optimizer Details: To efficiently train and validate the proposed model pipeline, different optimizers were tested in different stages. Four optimizers, Stochastic Gradient Descent (SGD), Adaptive Moment Estimation (Adam), Rectified Adaptive Moment Estimation (RAdam), and Adam with decoupled weight decay (AdamW) (43), were tested in the pre-training and fine-tuning segmentation phases. Through the tests, AdamW performed the best in both the pre-training and the fine-tuning phases, therefore, it was finally chosen for both the two phases.

For other hyperparameters and experiment implementations, this study generally follows the fine-tuned settings reported in (22, 24, 36).

E. Results

Various experiments were carried out to compare the model performance of the tested four transformer models, i.e., pure ViT, pure Swin Transformer (Swin-Trans), ViT variant with self-supervised pretraining (BEiT), and Swin Transformer with Uniform Masking (Swin-Trans-UM). The obtained results of treating the problem as an 8-class classification task are illustrated in **Figure 6** and **Table 1**.

From **Table 1**, it is evident that the significant differences in the number of fine-tuning epochs stem from the influence of the adopted MiM pre-training. The stopping criterion utilized in this study is AUC convergence. Specifically, fine-tuning is terminated when the improvement in AUC between consecutive evaluation epochs falls below a predefined threshold, signaling that the model's performance has stabilized.

With MiM pre-training, the Swin-Trans-UM and BEiT models converge in 15 epochs and 41 epochs, respectively. In contrast, without MiM pre-training, the original Vanilla ViT requires 40 epochs, and the original Vanilla Swin Transformer demands 280 epochs to converge.

The adoption of MiM pre-training considerably reduces the total number of fine-tuning epochs needed for convergence. This is achieved by equipping the model with rich, context-aware semantic features during pre-training, which provide a robust initialization for the downstream classification task. As a result, models with MiM pre-training not only converge faster but also maintain or improve their classification accuracy. This observed disparity underscores the efficiency and effectiveness of MiM pre-training in lowering computational requirements while delivering high performance.

Furthermore, regarding the primary and the most suitable overall model performance evaluation metric, AUC, both BEiT and Swin-Trans-UM outperform their variants without self-supervised pre-training, i.e., ViT and Swin-Trans. Especially, among the four models, Swin-Trans-UM obtains the best performance regarding Accuracy (94.77%), AUC (0.9743), Recall (0.8022), and F1-measure (0.7805).

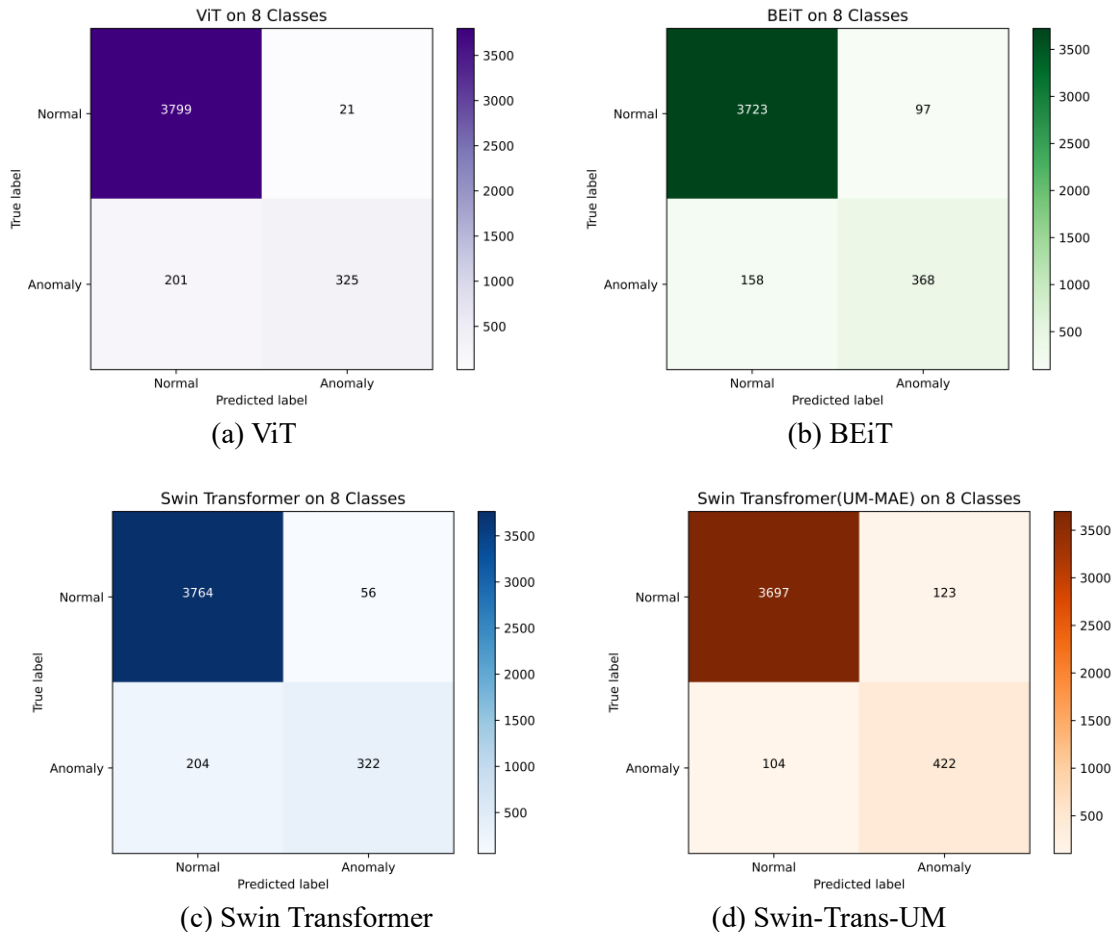


Figure 6 The testing results of the models visualized in confusion matrixes

Table 1 The model performance regarding different metrics

Model	Accuracy	AUC	Precision	Recall	F1-measure	Param (M)	Epoch time (s)	Number of fine-tuning Epoch
ViT	0.9489	0.9080	0.9393	0.6178	0.7454	632.20	4210	40
BEiT	0.9413	0.9481	0.7913	0.6996	0.7427	311.53	159	15
Swin-Trans	0.9401	0.9498	0.8518	0.6121	0.7123	86.90	120	280
Swin-Trans-UM	0.9477	0.9743	0.7743	0.8022	0.7805	194.95	223	41

ABLATION STUDY

It is easy to identify that the quantity of abnormal and normal image samples is highly imbalanced. To alleviate this imbalance, two ablation studies are carried out using the Swin-Trans-UM model, regarding the abnormal lane rendering detection not as the original 8-class multi-label classification problem but as a 2-class classification problem (Swin-Trans-UM_2 as the corresponding model) or 9-class multi-label classification problem (Swin-Trans-UM_9 as the corresponding model) in the fine-tuning process.

A. Treated as a 2-class classification

When treated as a 2-class image classification problem, all abnormal images are grouped as one class, and together with the normal class, there are 2 classes in the fine-tuning process. In this way, the

imbalance between the classes is alleviated since grouping abnormal classes together reduces the disparity between the number of normal instances and anomalies. By consolidating the abnormal classes into a single group, the number of anomaly-related instances is less sparse, making the distribution more balanced compared to treating each anomaly type separately.

The results of the tested Swin-Trans-UM_2 model performance under this setting are demonstrated in **Figure 7 (a)** and **Table 2**. It is evident that all the reported evaluation metrics (i.e., Accuracy, AUC, Precision, Recall, F1-measure) for Swin-Trans-UM_2 are improved compared to the original approach, which treats the problem as an 8-class classification (Swin-Trans-UM_8).

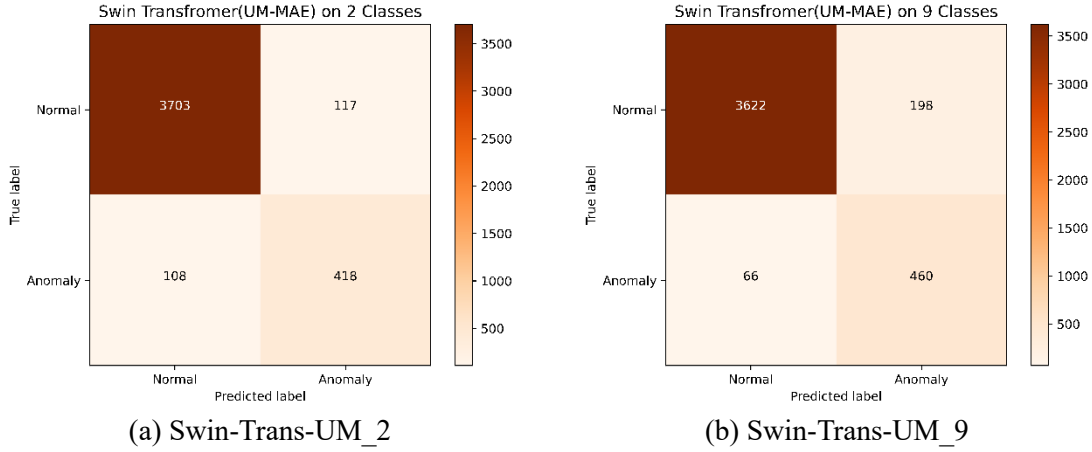


Figure 7 The confusion matrix of Swin-Trans-UM when treated as a 2-class classification and a 9-class multi-label classification

B. Treated as a 9-class multi-label classification

When treated as a 9-class multi-label image classification problem, all abnormal images are grouped as one extra integrated class while still keeping each sub-abnormal class as in the dataset. Thus 9 classes are obtained and each abnormal instance will get at least two class labels. In this way, the imbalance between the classes is further alleviated. The results of the tested Swin-Trans-UM_9 model performance under this setting are demonstrated in **Figure 7 (b)** and **Table 2**. All evaluation metrics of Swin-Trans-UM_9 are degraded compared with the original approach treated as an 8-class classification problem (Swin-Trans-UM_8). This might be due to the extra label for each abnormal instance confusing the model during the fine-tuning process when updating the model weights by backpropagation. Detailed reasons need further study.

Table 2 The performance of the Swin-Trans-UM_2 and Swin-Trans-UM_9

Model	Accuracy	AUC	Precision	Recall	F1-measure
Swin-Trans-UM_2	0.9482	0.9756	0.7813	0.7947	0.7879
Swin-Trans-UM_9	0.9392	0.9731	0.6990	0.8745	0.7770
Swin-Trans-UM_8	0.9477	0.9743	0.7743	0.8022	0.7805

CONCLUSIONS, LIMITATIONS, AND FUTURE RESEARCH

Lane rendering is an important element in digital maps used for navigation services and other traffic-related applications. However, there might be anomalies in the lane rendering images. To accurately and effectively detect the anomalies, this paper converts the problem of lane rendering image anomaly detection to a classification problem, which allows various state-of-the-art computer vision techniques to

be applicable. Furthermore, this paper proposes a four-phase pipeline consisting of data pre-processing, self-supervised pre-training with the masked image modeling (MiM) method, customized fine-tuning using cross-entropy loss with label smoothing, and post-processing. Various metrics are adopted to evaluate the model performance. Extensive experiments have demonstrated that the proposed pipeline effectively addresses the lane rendering image anomaly detection task, achieving outstanding performance in terms of high accuracy. And especially, the self-supervised pre-training with MiM can greatly improve the model accuracy, e.g., Swin Transformer with Uniform Masking as self-supervised pretraining (Swin-Trans-UM) obtained better accuracy at 94.77% and better AUC at 0.9743 compared with the pure Swin Transformer without pre-training (Swin-Trans) whose accuracy is 94.01%, AUC is 0.9498, while significantly reducing the model fine-tuning time, e.g., Swin-Trans-UM reduced the number of epochs of Swin-Trans at 280 to only 41. Ablation study regarding techniques to alleviate the data imbalance between normal and abnormal instances further enhances the model performance, with the 2-class classification variant of the Swin-Trans-UM model, i.e., Swin-Trans-UM_2 obtained the best performance on all the evaluation metrics, i.e., Accuracy (94.82%), AUC (0.9756), Precision (0.7813), Recall (0.7947), and F1-measure (0.7879). Lastly, regarding the societal benefits, the proposed method can improve the efficiency of lane rendering image data anomaly detection reducing labor costs while keeping high accuracy.

As for limitations, due to the unavailability of other relevant datasets, this study only examined and evaluated the proposed method and results on a single dataset, which might potentially constrain the generalizability of the proposed method and corresponding results. Furthermore, limited by the properties of the data, the focus of this study is confined to discerning whether the lane rendering image is abnormal or normal. Further investigation into checking and diagnosing the specific anomaly types, as well as locating the anomalies within the images, could be intriguing directions for future studies. This would involve more detailed anomaly segmentation, which could provide valuable deeper insights into the nature and causes of detected abnormalities. However, achieving such advancements would necessitate access to structured datasets equipped with labeled segmentation maps to facilitate robust anomaly localization and classification tasks.

Moreover, certain anomaly images in the dataset have multiple labels, a complexity that this study did not address. Future studies should explore methods for handling multi-label classification to account for overlapping or co-occurring anomalies. Techniques such as multi-label learning algorithms (44), label correlation modeling (45, 46), or hierarchical classification approaches (47) could be explored to tackle this issue. Addressing multi-label scenarios would enhance the robustness and applicability of anomaly detection systems in real-world contexts.

Lastly, the current study employs a supervised approach during the fine-tuning phase, necessitating high-quality ground truth labels. Future studies could explore the potential of semi-supervised or unsupervised machine learning approaches to distinguish anomalies from normal instances without relying on extensive labeled data. For example, Contrastive Language-Image Pre-training (CLIP) (48) can perform zero-shot classification by learning from large-scale, unannotated data, aligning images with textual descriptions. Similarly, Bootstrapping Language-Image Pre-training (BLIP) (49) can effectively perform image-text matching tasks in a self-supervised manner, which could help classify anomalies with minimal reliance on labeled data.

ACKNOWLEDGMENTS

This work was supported by the Applied and Technical Sciences (TTW), a subdomain of the Dutch Institute for Scientific Research (NWO) through the Project *Safe and Efficient Operation of Automated and Human-Driven Vehicles in Mixed Traffic* (SAMEN) under Contract 17187. The authors thank the [2022 Global AI Challenge](#) for providing the original data.

Note

Author Contributions

The authors confirm contribution to the paper as follows: study conception and design: Y. Dong, X. Lu; data collection: Y. Dong, X. Lu, and R. Li; analysis and interpretation of results: Y. Dong, X. Lu,

R. Li, and H. Farah; draft manuscript preparation: Y. Dong, X. Lu, R. Li, W. Song, B. van Arem, and H. Farah. All authors reviewed the results and approved the final version of the manuscript.

Declaration of Conflicting Interests

The author(s) have disclosed no potential conflicts of interest related to the research, authorship, or publication of this article.

REFERENCES

1. Yang, L., Y. Bian, X. Zhao, X. Liu, and X. Yao. Drivers' Acceptance of Mobile Navigation Applications: An Extended Technology Acceptance Model Considering Drivers' Sense of Direction, Navigation Application Affinity and Distraction Perception. *International Journal of Human Computer Studies*, 2021. <https://doi.org/10.1016/j.ijhcs.2020.102507>.
2. Vörös, F., G. Gartner, M. P. Peterson, and B. Kovács. What Does the Ideal Built-In Car Navigation System Look Like?—An Investigation in the Central European Region. *Applied Sciences (Switzerland)*, Vol. 12, No. 8, 2022. <https://doi.org/10.3390/app12083716>.
3. Barsi, M., and A. Barsi. Topological Anomaly Detection In Automotive Simulator Maps. *The International Archives of the Photogrammetry, Remote Sensing and Spatial Information Sciences* 43, pp.343-348, 2022.
4. Elghazaly, G., R. Frank, S. Harvey, and S. Safko. High-Definition Maps: Comprehensive Survey, Challenges, and Future Perspectives. *IEEE Open Journal of Intelligent Transportation Systems*, 2023. <https://doi.org/10.1109/OJITS.2023.3295502>.
5. Dib, J., K. Sirlantzis, and G. Howells. A Review on Negative Road Anomaly Detection Methods. *IEEE Access*, 2020. <https://doi.org/10.1109/ACCESS.2020.2982220>.
6. Luo, D., J. Lu, and G. Guo. Road Anomaly Detection through Deep Learning Approaches. *IEEE Access*, 2020. <https://doi.org/10.1109/ACCESS.2020.3004590>.
7. Cao, W., Q. Liu, and Z. He. Review of Pavement Defect Detection Methods. *IEEE Access*, 2020. <https://doi.org/10.1109/aCCESS.2020.2966881>.
8. Tong, Z., D. Yuan, J. Gao, and Z. Wang. Pavement Defect Detection with Fully Convolutional Network and an Uncertainty Framework. *Computer-Aided Civil and Infrastructure Engineering*, 2020. <https://doi.org/10.1111/mice.12533>.
9. Sun, Y., H. Tang, and H. Zhang. Automatic Detection of Pavement Marking Defects in Road Inspection Images Using Deep Learning. *Journal of Performance of Constructed Facilities*, 2024. <https://doi.org/10.1061/jpcfey.cfeng-4619>.
10. Ruiz, A. L., and H. Alzraiee. Automated Pavement Marking Defects Detection. In *ISARC. Proceedings of the International Symposium on Automation and Robotics in Construction* (Vol. 37, pp. 67-73). IAARC Publications. 2020.
11. Nguyen, T. S., M. Avila, and S. Begot. Automatic Detection and Classification of Defect on Road Pavement Using Anisotropy Measure. In 2009 17th European Signal Processing Conference (pp. 617-621). IEEE. 2009.
12. NCUTCD. *Manual on Uniform Traffic Control Devices for Streets and Highways - MUTCD - 11th Edition* 2024.
13. Ministry of Transport of the People's Republic of China. Specifications for Highway Geometric Design (JTG D20—2017). *Industry Standards of the People's Republic of China*, 2018, pp. 1–271.
14. Bello-Salau, H., A. J. Onumanyi, A. T. Salawudeen, M. B. Mu'Azur, and A. M. Oyinbo. An Examination of Different Vision Based Approaches for Road Anomaly Detection. In *2019 2nd International Conference of the IEEE Nigeria Computer Chapter (NigeriaComputConf)* (pp. 1-6). IEEE 2019.
15. Zhang, H., S. Zhao, R. Liu, W. Wang, Y. Hong, and R. Hu. Automatic Traffic Anomaly Detection on the Road Network with Spatial-Temporal Graph Neural Network Representation Learning. *Wireless Communications and Mobile Computing*, 2022. <https://doi.org/10.1155/2022/4222827>.
16. Santhosh K. K., Dogra D. P., Roy P. P., Anomaly detection in road traffic using visual surveillance: A survey. *ACM Computing Surveys (CSUR)*. 2020, 53(6):1-26.
17. Rajbahadur, G. K., A. J. Malton, A. Walenstein, and A. E. Hassan. A Survey of Anomaly Detection for Connected Vehicle Cybersecurity and Safety. In *2018 IEEE Intelligent Vehicles Symposium (IV)*, pp. 421-426. IEEE, 2018.
18. Dong, Y., K. Chen, Y. Peng, and Z. Ma. Comparative Study on Supervised versus Semi-Supervised Machine Learning for Anomaly Detection of In-Vehicle CAN Network. In *2022 IEEE 25th International Conference on Intelligent Transportation Systems (ITSC)*, pp. 2914-2919. IEEE. 2022.

19. Hou, M., M. Wang, W. Zhao, Q. Ni, Z. Cai, and X. Kong. A Lightweight Framework for Abnormal Driving Behavior Detection. *Computer Communications*, Vol. 184, No. May 2021, 2022, pp. 128–136. <https://doi.org/10.1016/j.comcom.2021.12.007>.
20. Hu, J., X. Zhang, and S. Maybank. Abnormal Driving Detection with Normalized Driving Behavior Data: A Deep Learning Approach. *IEEE Transactions on Vehicular Technology*, Vol. 69, No. 7, 2020, pp. 6943–6951. <https://doi.org/10.1109/TVT.2020.2993247>.
21. Zhang, L., Y. Dong, H. Farah, A. Zgonnikov, and B. Van Arem. Data-Driven Semi-Supervised Machine Learning with Surrogate Safety Measures for Abnormal Driving Behavior Detection. No. August, 2023, pp. 1–19. <https://doi.org/https://doi.org/10.48550/arXiv.2312.04610>.
22. Bao, H., L. Dong, S. Piao, and F. Wei. BEIT: Bert Pre-Training Of Image Transformers. In *International Conference on Learning Representations*. 2022.
23. El-Nouby, A., G. Izacard, H. Touvron, I. Laptev, H. Jegou, and E. Grave. Are Large-Scale Datasets Necessary for Self-Supervised Pre-Training? *arXiv preprint arXiv:2112.10740*, 2021.
24. He, K., X. Chen, S. Xie, Y. Li, P. Dollar, and R. Girshick. Masked Autoencoders Are Scalable Vision Learners. In *Proceedings of the IEEE/CVF Conference on Computer Vision And Pattern Recognition*, pp. 16000-16009. 2022.
25. Xie, Z., Z. Zhang, Y. Cao, Y. Lin, J. Bao, Z. Yao, Q. Dai, and H. Hu. SimMIM: A Simple Framework for Masked Image Modeling. In *Proceedings of the IEEE/CVF Conference on Computer Vision and Pattern Recognition*, pp. 9653-9663. 2022.
26. Li, R., and Y. Dong. Robust Lane Detection Through Self Pre-Training With Masked Sequential Autoencoders and Fine-Tuning With Customized PolyLoss. *IEEE Transactions on Intelligent Transportation Systems*, Vol. 24, No. 12, 2023, pp. 14121–14132. <https://doi.org/10.1109/TITS.2023.3305015>.
27. Bergmann, P., M. Fauser, D. Sattlegger, and C. Steger. MVTEC Ad-A Comprehensive Real-World Dataset for Unsupervised Anomaly Detection. In *Proceedings of the IEEE/CVF conference on computer vision and pattern recognition*, pp. 9592-9600. 2019.
28. Yan, X., H. Zhang, X. Xu, X. Hu, and P. A. Heng. Learning Semantic Context from Normal Samples for Unsupervised Anomaly Detection. *35th AAAI Conference on Artificial Intelligence, AAAI 2021*, Vol. 4A, 2021, pp. 3110–3118. <https://doi.org/10.1609/aaai.v35i4.16420>.
29. Deecke, L., R. Vandermeulen, L. Ruff, S. Mandt, and M. Kloft. Image Anomaly Detection with Generative Adversarial Networks. In *Machine Learning and Knowledge Discovery in Databases: European Conference, ECML PKDD 2018, Dublin, Ireland, September 10–14, 2018, Proceedings, Part I 18* (pp. 3-17). Springer International Publishing. 2019.
30. Kwon, G., M. Prabhushankar, D. Temel, and G. AlRegib. *Backpropagated Gradient Representations for Anomaly Detection*. Springer International Publishing, 2020.
31. Bogdoll, D., M. Nitsche, and J. M. Zollner. Anomaly Detection in Autonomous Driving: A Survey. *IEEE Computer Society Conference on Computer Vision and Pattern Recognition Workshops*, Vol. 2022-June, 2022, pp. 4487–4498. <https://doi.org/10.1109/CVPRW56347.2022.00495>.
32. Yang, J., R. Xu, Z. Qi, and Y. Shi. Visual Anomaly Detection for Images: A Systematic Survey. *Procedia Computer Science*, Vol. 199, No. 2021, 2021, pp. 471–478. <https://doi.org/10.1016/j.procs.2022.01.057>.
33. Parmar, N., A. Vaswani, J. Uszkoreit, L. Kaiser, N. Shazeer, A. Ku, and D. Tran. Image Transformer. In *International Conference on Machine Learning* (pp. 4055-4064). PMLR. 2018.
34. Liu, Z., Y. Lin, Y. Cao, H. Hu, Y. Wei, Z. Zhang, S. Lin, and B. Guo. Swin Transformer: Hierarchical Vision Transformer Using Shifted Windows. *2021 IEEE/CVF International Conference on Computer Vision (ICCV)*, 2021, pp. 9992–10002.
35. Guo, M. H., T. X. Xu, J. J. Liu, Z. N. Liu, P. T. Jiang, T. J. Mu, S. H. Zhang, R. R. Martin, M. M. Cheng, and S. M. Hu. Attention Mechanisms in Computer Vision: A Survey. *Computational Visual Media*, Vol. 8, No. 3, 2022, pp. 331–368. <https://doi.org/10.1007/s41095-022-0271-y>.
36. Li, X., W. Wang, L. Yang, and J. Yang. Uniform Masking: Enabling MAE Pre-Training for Pyramid-Based Vision Transformers with Locality. *arXiv preprint arXiv:2205.10063*, 2022.

37. Dosovitskiy, A., L. Beyer, A. Kolesnikov, D. Weissenborn, X. Zhai, T. Unterthiner, M. Dehghani, M. Minderer, G. Heigold, S. Gelly, J. Uszkoreit, and N. Houlsby. An Image Is Worth 16x16 Words: Transformers For Image Recognition At Scale. In *International Conference on Learning Representations*. 2020.
38. Ramesh, A., M. Pavlov, G. Goh, S. Gray, C. Voss, A. Radford, M. Chen, and I. Sutskever. Zero-Shot Text-to-Image Generation. 2021. In *International Conference on Machine Learning*. 2021, (pp. 8821-8831). PMLR.
39. Chen, M., A. Radford, R. Child, J. Wu, H. Jun, D. Luan, and I. Sutskever. Generative Pretraining from Pixels. 2020. In *International conference on machine learning*. 2020 (pp. 1691-1703). PMLR.
40. Wang, W., E. Xie, X. Li, D. P. Fan, K. Song, D. Liang, T. Lu, P. Luo, and L. Shao. Pyramid Vision Transformer: A Versatile Backbone for Dense Prediction without Convolutions. 2021. In *International conference on machine learning*. 2020 (pp. 1691-1703). PMLR.
41. Bao, H., L. Dong, and F. Wei. Beit: Bert Pre-Training of Image Transformers. In *International Conference on Learning Representations*, 2021.
42. Zhang, H., M. Cisse, Y. N. Dauphin, and D. Lopez-Paz. MixUp: Beyond Empirical Risk Minimization. *6th International Conference on Learning Representations, ICLR 2018 - Conference Track Proceedings*, 2018, pp. 1–13.
43. Loshchilov, I., and F. Hutter. Decoupled Weight Decay Regularization. 2019. arXiv preprint arXiv:1711.05101. 2017.
44. Zhang, M. L., and Z. H. Zhou. A Review on Multi-Label Learning Algorithms. *IEEE Transactions on Knowledge and Data Engineering*. 2013. 26(8):1819-37.
45. Zhu, Y., J. T. Kwok, and Z. H. Zhou. Multi-Label Learning with Global and Local Label Correlation. *IEEE Transactions on Knowledge and Data Engineering*, 2018. <https://doi.org/10.1109/TKDE.2017.2785795>.
46. Yu, Y., W. Pedrycz, and D. Miao. Multi-Label Classification by Exploiting Label Correlations. *Expert Systems with Applications*, 2014. <https://doi.org/10.1016/j.eswa.2013.10.030>.
47. Wehrmann, J., R. Cerri, and R. C. Barros. Hierarchical Multi-Label Classification Networks. 2018. In *International Conference on Machine Learning 2018*, (pp. 5075-5084). PMLR.
48. Radford, A., J. W. Kim, C. Hallacy, A. Ramesh, G. Goh, S. Agarwal, G. Sastry, A. Askell, P. Mishkin, J. Clark, G. Krueger, and I. Sutskever. Learning Transferable Visual Models From Natural Language Supervision. In *International conference on machine learning*. 2021, (pp. 8748-8763). PMLR.
49. Li, J., D. Li, C. Xiong, and S. Hoi. BLIP: Bootstrapping Language-Image Pre-Training for Unified Vision-Language Understanding and Generation. In *International Conference on Machine Learning 2022*, (pp. 12888-12900). PMLR.

APPENDIX

Note: The following neural network structures are based upon 8-class classification in the fine-tuning phase. There are a few minor differences regarding the output layers for the models used in the self-supervised pretraining phase or for the 2-class and 9-class classifications.

Multiply-Add, short for multiply-accumulate operation, which means computing the product of two numbers and adding that product to an accumulator. It is used as shorthand for the total number of operations in the model as popular layers such as convolution and linear layers multiply weights with inputs and then add the results of the multiplication (possibly with a bias).

TABLE A1 Parameter settings for each layer of Vision Transformer

Layer	Kernel Shape	Input Shape	Output Shape	Param	Mult-Adds
VisionTransformer	--	[1, 3, 224, 224]	[1, 8]	253,440	--
PatchEmbed	--	[1, 3, 224, 224]	[1, 196, 1280]	--	--
Conv2d	[16, 16]	[1, 3, 224, 224]	[1, 1280, 14, 14]	984,320	192,926,720
Dropout	--	[1, 197, 1280]	[1, 197, 1280]	--	--
ModuleList (Consisting of 32 Blocks with the same structure as below)					
Block 1-32	--	[1, 197, 1280]	[1, 197, 1280]	--	--
LayerNorm	--	[1, 197, 1280]	[1, 197, 1280]	2,560	2,560
Attention	--	[1, 197, 1280]	[1, 197, 1280]	6,554,880	6,554,880
Identity	--	[1, 197, 1280]	[1, 197, 1280]	--	--
LayerNorm	--	[1, 197, 1280]	[1, 197, 1280]	2,560	2,560
Mlp	--	[1, 197, 1280]	[1, 197, 1280]	13,113,600	13,113,600
Identity	--	[1, 197, 1280]	[1, 197, 1280]	--	--
LayerNorm	--	[1, 197, 1280]	[1, 197, 1280]	2,560	2,560
Linear	--	[1, 1280]	[1, 8]	10,248	10,248

TABLE A2 Parameter settings for each layer of BEiT

Layer	Kernel Shape	Input Shape	Output Shape	Param	Mult-Adds
BEiT	--	[1, 3, 224, 224]	[1, 8]	768	--
PatchEmbed	--	[1, 3, 224, 224]	[1, 196, 768]	--	--
Conv2d	[16, 16]	[1, 3, 224, 224]	[1, 768, 14, 14]	590,592	115,756,032
Dropout	--	[1, 197, 768]	[1, 197, 768]	--	--
ModuleList (Consisting of 12 Blocks with the same structure as below)					
Block 1-12	--	[1, 197, 768]	[1, 197, 768]	1,536	--
LayerNorm	--	[1, 197, 768]	[1, 197, 768]	1,536	1,536
Attention	--	[1, 197, 768]	[1, 197, 768]	2,370,384	590,592
Identity	--	[1, 197, 768]	[1, 197, 768]	--	--
LayerNorm	--	[1, 197, 768]	[1, 197, 768]	1,536	1,536
Mlp	--	[1, 197, 768]	[1, 197, 768]	4,722,432	4,722,432
Identity	--	[1, 197, 768]	[1, 197, 768]	--	--
Identity	--	[1, 197, 768]	[1, 197, 768]	--	--
LayerNorm	--	[1, 768]	[1, 768]	1,536	1,536
Linear	--	[1, 768]	[1, 8]	6,152	6,152

TABLE A3 Parameter settings for each layer of Swin Transformer

Layer (type:depth-idx)	Kernel Shape	Input Shape	Output Shape	Param	Mult-Adds
SwinTransformerV2	--	[1, 3, 256, 256]	[1, 8]	--	--
PatchEmbed	--	[1, 3, 256, 256]	[1, 4096, 96]	--	--
Conv2d	[4, 4]	[1, 3, 256, 256]	[1, 96, 64, 64]	4,704	19,267,584
LayerNorm	--	[1, 4096, 96]	[1, 4096, 96]	192	192
Dropout	--	[1, 4096, 96]	[1, 4096, 96]	--	--
ModuleList					
BasicLayer	--	[1, 4096, 96]	[1, 1024, 192]	--	--
ModuleList	--	--	--	--	--
SwinTransformerBlock	--	[1, 4096, 96]	[1, 4096, 96]	114,819	673,632
SwinTransformerBlock	--	[1, 4096, 96]	[1, 4096, 96]	114,819	673,632
PatchMerging	--	[1, 4096, 96]	[1, 1024, 192]	--	--
Linear	--	[1, 1024, 384]	[1, 1024, 192]	73,728	73,728
LayerNorm	--	[1, 1024, 192]	[1, 1024, 192]	384	384
BasicLayer	--	[1, 1024, 192]	[1, 256, 384]	--	--
ModuleList	--	--	--	--	--
SwinTransformerBlock	--	[1, 1024, 192]	[1, 1024, 192]	449,286	894,144
SwinTransformerBlock	--	[1, 1024, 192]	[1, 1024, 192]	449,286	894,144
PatchMerging	--	[1, 1024, 192]	[1, 256, 384]	--	--
Linear	--	[1, 256, 768]	[1, 256, 384]	294,912	294,912
LayerNorm	--	[1, 256, 384]	[1, 256, 384]	768	768
BasicLayer	--	[1, 256, 384]	[1, 64, 768]	--	--
ModuleList	--	--	--	--	--
SwinTransformerBlock	--	[1, 256, 384]	[1, 256, 384]	1,781,772	1,782,144
SwinTransformerBlock	--	[1, 256, 384]	[1, 256, 384]	1,781,772	1,782,144
SwinTransformerBlock	--	[1, 256, 384]	[1, 256, 384]	1,781,772	1,782,144
SwinTransformerBlock	--	[1, 256, 384]	[1, 256, 384]	1,781,772	1,782,144
SwinTransformerBlock	--	[1, 256, 384]	[1, 256, 384]	1,781,772	1,782,144
SwinTransformerBlock	--	[1, 256, 384]	[1, 256, 384]	1,781,772	1,782,144
PatchMerging	--	[1, 256, 384]	[1, 64, 768]	--	--
Linear	--	[1, 64, 1536]	[1, 64, 768]	1,179,648	1,179,648
LayerNorm	--	[1, 64, 768]	[1, 64, 768]	1,536	1,536
BasicLayer	--	[1, 64, 768]	[1, 64, 768]	--	--
ModuleList	--	--	--	--	--
SwinTransformerBlock	--	[1, 64, 768]	[1, 64, 768]	7,100,952	5,329,920
SwinTransformerBlock	--	[1, 64, 768]	[1, 64, 768]	7,100,952	5,329,920
LayerNorm	--	[1, 64, 768]	[1, 64, 768]	1,536	1,536
AdaptiveAvgPool1d	--	[1, 768, 64]	[1, 768, 1]	--	--
Linear	--	[1, 768]	[1, 8]	6,152	6,152

TABLE A4 Parameter settings for each layer of the Swin Transformer with Uniform Masking

Layer (type: depth-idx)	Kernel Shape	Input Shape	Output Shape	Param	Multi-Adds
Swin (Swin)	--	[1, 3, 256, 256]	[1, 8]	--	--
PatchEmbed (patch embed): 1-1	--	[1, 3, 256, 256]	[1, 4096, 192]	--	--
Conv2d (proj): 2-1	[4, 4]	[1, 3, 256, 256]	[1, 192, 64, 64]	9,408	38,535,168
LayerNorm (norm): 2-2	--	[1, 4096, 192]	[1, 4096, 192]	384	384
ModuleList (blocks): 1-2	--	--	--	--	--
SwinBlock (0): 2-3	--	[1, 4096, 192]	[1, 4096, 192]	--	--
LayerNorm (norm1): 3-1	--	[1, 4096, 192]	[1, 4096, 192]	384	384
WindowAttention (attn): 3-2	--	[16, 256, 192]	[16, 256, 192]	148,806	612,642,816
Identity (drop path): 3-3	--	[1, 4096, 192]	[1, 4096, 192]	--	--
LayerNorm (norm2): 3-4	--	[1, 4096, 192]	[1, 4096, 192]	384	384
Mlp (mlp): 3-5	--	[1, 4096, 192]	[1, 4096, 192]	295,872	295,872
Identity (drop path): 3-6	--	[1, 4096, 192]	[1, 4096, 192]	--	--
SwinBlock (1): 2-4	--	[1, 4096, 192]	[1, 4096, 192]	--	--
LayerNorm (norm1): 3-7	--	[1, 4096, 192]	[1, 4096, 192]	384	384
WindowAttention (attn): 3-8	--	[16, 256, 192]	[16, 256, 192]	148,806	612,642,816
DropPath (drop path): 3-9	--	[1, 4096, 192]	[1, 4096, 192]	--	--
LayerNorm (norm2): 3-10	--	[1, 4096, 192]	[1, 4096, 192]	384	384
Mlp (mlp): 3-11	--	[1, 4096, 192]	[1, 4096, 192]	295,872	295,872
DropPath (drop path): 3-12	--	[1, 4096, 192]	[1, 4096, 192]	--	--
SwinBlock (2): 2-5	--	[1, 4096, 192]	[1, 1024, 384]	--	--
PatchMerge (downsample): 3-13	--	[1, 4096, 192]	[1, 1024, 384]	295,680	302,383,488
LayerNorm (norm1): 3-14	--	[1, 1024, 384]	[1, 1024, 384]	768	768
WindowAttention (attn): 3-15	--	[4, 256, 384]	[4, 256, 384]	592,332	257,169,408
DropPath (drop path): 3-16	--	[1, 1024, 384]	[1, 1024, 384]	--	--
LayerNorm (norm2): 3-17	--	[1, 1024, 384]	[1, 1024, 384]	768	768
Mlp (mlp): 3-18	--	[1, 1024, 384]	[1, 1024, 384]	1,181,568	1,181,568
DropPath (drop path): 3-19	--	[1, 1024, 384]	[1, 1024, 384]	--	--
SwinBlock (3): 2-6	--	[1, 1024, 384]	[1, 1024, 384]	--	--
LayerNorm (norm1): 3-20	--	[1, 1024, 384]	[1, 1024, 384]	768	768
WindowAttention (attn): 3-21	--	[4, 256, 384]	[4, 256, 384]	592,332	257,169,408
DropPath (drop path): 3-22	--	[1, 1024, 384]	[1, 1024, 384]	--	--
LayerNorm (norm2): 3-23	--	[1, 1024, 384]	[1, 1024, 384]	768	768
Mlp (mlp): 3-24	--	[1, 1024, 384]	[1, 1024, 384]	1,181,568	1,181,568
DropPath (drop path): 3-25	--	[1, 1024, 384]	[1, 1024, 384]	--	--
SwinBlock (4): 2-7	--	[1, 1024, 384]	[1, 256, 768]	--	--
PatchMerge (downsample): 3-26	--	[1, 1024, 384]	[1, 256, 768]	1,181,184	302,187,264
LayerNorm (norm1): 3-27	--	[1, 256, 768]	[1, 256, 768]	1,536	1,536
WindowAttention (attn): 3-28	--	[1, 256, 768]	[1, 256, 768]	2,364,120	117,181,440
DropPath (drop path): 3-29	--	[1, 256, 768]	[1, 256, 768]	--	--
LayerNorm (norm2): 3-30	--	[1, 256, 768]	[1, 256, 768]	1,536	1,536
Mlp (mlp): 3-31	--	[1, 256, 768]	[1, 256, 768]	4,722,432	4,722,432
DropPath (drop path): 3-32	--	[1, 256, 768]	[1, 256, 768]	--	--
SwinBlock (5): 2-8	--	[1, 256, 768]	[1, 256, 768]	--	--
LayerNorm (norm1): 3-33	--	[1, 256, 768]	[1, 256, 768]	1,536	1,536
WindowAttention (attn): 3-34	--	[1, 256, 768]	[1, 256, 768]	2,364,120	117,181,440
DropPath (drop path): 3-35	--	[1, 256, 768]	[1, 256, 768]	--	--
LayerNorm (norm2): 3-36	--	[1, 256, 768]	[1, 256, 768]	1,536	1,536
Mlp (mlp): 3-37	--	[1, 256, 768]	[1, 256, 768]	4,722,432	4,722,432
DropPath (drop path): 3-38	--	[1, 256, 768]	[1, 256, 768]	--	--
SwinBlock (6): 2-9	--	[1, 256, 768]	[1, 256, 768]	--	--
LayerNorm (norm1): 3-39	--	[1, 256, 768]	[1, 256, 768]	1,536	1,536
WindowAttention (attn): 3-40	--	[1, 256, 768]	[1, 256, 768]	2,364,120	117,181,440
DropPath (drop path): 3-41	--	[1, 256, 768]	[1, 256, 768]	--	--

LayerNorm (norm2): 3-90	--	[1, 256, 768]	[1, 256, 768]	1,536	1,536
Mlp (mlp): 3-91	--	[1, 256, 768]	[1, 256, 768]	4,722,432	4,722,432
DropPath (drop path): 3-92	--	[1, 256, 768]	[1, 256, 768]	--	--
SwinBlock (15): 2-18	--	[1, 256, 768]	[1, 256, 768]	--	--
LayerNorm (norm1): 3-93	--	[1, 256, 768]	[1, 256, 768]	1,536	1,536
WindowAttention (attn): 3-94	--	[1, 256, 768]	[1, 256, 768]	2,364,120	117,181,440
DropPath (drop path): 3-95	--	[1, 256, 768]	[1, 256, 768]	--	--
LayerNorm (norm2): 3-96	--	[1, 256, 768]	[1, 256, 768]	1,536	1,536
Mlp (mlp): 3-97	--	[1, 256, 768]	[1, 256, 768]	4,722,432	4,722,432
DropPath (drop path): 3-98	--	[1, 256, 768]	[1, 256, 768]	--	--
SwinBlock (16): 2-19	--	[1, 256, 768]	[1, 256, 768]	--	--
LayerNorm (norm1): 3-99	--	[1, 256, 768]	[1, 256, 768]	1,536	1,536
WindowAttention (attn): 3-100	--	[1, 256, 768]	[1, 256, 768]	2,364,120	117,181,440
DropPath (drop path): 3-101	--	[1, 256, 768]	[1, 256, 768]	--	--
LayerNorm (norm2): 3-102	--	[1, 256, 768]	[1, 256, 768]	1,536	1,536
Mlp (mlp): 3-103	--	[1, 256, 768]	[1, 256, 768]	4,722,432	4,722,432
DropPath (drop path): 3-104	--	[1, 256, 768]	[1, 256, 768]	--	--
SwinBlock (17): 2-20	--	[1, 256, 768]	[1, 256, 768]	--	--
LayerNorm (norm1): 3-105	--	[1, 256, 768]	[1, 256, 768]	1,536	1,536
WindowAttention (attn): 3-106	--	[1, 256, 768]	[1, 256, 768]	2,364,120	117,181,440
DropPath (drop path): 3-107	--	[1, 256, 768]	[1, 256, 768]	--	--
LayerNorm (norm2): 3-108	--	[1, 256, 768]	[1, 256, 768]	1,536	1,536
Mlp (mlp): 3-109	--	[1, 256, 768]	[1, 256, 768]	4,722,432	4,722,432
DropPath (drop path): 3-110	--	[1, 256, 768]	[1, 256, 768]	--	--
SwinBlock (18): 2-21	--	[1, 256, 768]	[1, 256, 768]	--	--
LayerNorm (norm1): 3-111	--	[1, 256, 768]	[1, 256, 768]	1,536	1,536
WindowAttention (attn): 3-112	--	[1, 256, 768]	[1, 256, 768]	2,364,120	117,181,440
DropPath (drop path): 3-113	--	[1, 256, 768]	[1, 256, 768]	--	--
LayerNorm (norm2): 3-114	--	[1, 256, 768]	[1, 256, 768]	1,536	1,536
Mlp (mlp): 3-115	--	[1, 256, 768]	[1, 256, 768]	4,722,432	4,722,432
DropPath (drop path): 3-116	--	[1, 256, 768]	[1, 256, 768]	--	--
SwinBlock (19): 2-22	--	[1, 256, 768]	[1, 256, 768]	--	--
LayerNorm (norm1): 3-117	--	[1, 256, 768]	[1, 256, 768]	1,536	1,536
WindowAttention (attn): 3-118	--	[1, 256, 768]	[1, 256, 768]	2,364,120	117,181,440
DropPath (drop path): 3-119	--	[1, 256, 768]	[1, 256, 768]	--	--
LayerNorm (norm2): 3-120	--	[1, 256, 768]	[1, 256, 768]	1,536	1,536
Mlp (mlp): 3-121	--	[1, 256, 768]	[1, 256, 768]	4,722,432	4,722,432
DropPath (drop path): 3-122	--	[1, 256, 768]	[1, 256, 768]	--	--
SwinBlock (20): 2-23	--	[1, 256, 768]	[1, 256, 768]	--	--
LayerNorm (norm1): 3-123	--	[1, 256, 768]	[1, 256, 768]	1,536	1,536
WindowAttention (attn): 3-124	--	[1, 256, 768]	[1, 256, 768]	2,364,120	117,181,440
DropPath (drop path): 3-125	--	[1, 256, 768]	[1, 256, 768]	--	--
LayerNorm (norm2): 3-126	--	[1, 256, 768]	[1, 256, 768]	1,536	1,536
Mlp (mlp): 3-127	--	[1, 256, 768]	[1, 256, 768]	4,722,432	4,722,432
DropPath (drop path): 3-128	--	[1, 256, 768]	[1, 256, 768]	--	--
SwinBlock (21): 2-24	--	[1, 256, 768]	[1, 256, 768]	--	--
LayerNorm (norm1): 3-129	--	[1, 256, 768]	[1, 256, 768]	1,536	1,536
WindowAttention (attn): 3-130	--	[1, 256, 768]	[1, 256, 768]	2,364,120	117,181,440
DropPath (drop path): 3-131	--	[1, 256, 768]	[1, 256, 768]	--	--
LayerNorm (norm2): 3-132	--	[1, 256, 768]	[1, 256, 768]	1,536	1,536
Mlp (mlp): 3-133	--	[1, 256, 768]	[1, 256, 768]	4,722,432	4,722,432
DropPath (drop path): 3-134	--	[1, 256, 768]	[1, 256, 768]	--	--
SwinBlock (22): 2-25	--	[1, 256, 768]	[1, 64, 1536]	--	--
PatchMerge (downsample): 3-135	--	[1, 256, 768]	[1, 64, 1536]	4,721,664	302,089,728
LayerNorm (norm1): 3-136	--	[1, 64, 1536]	[1, 64, 1536]	3,072	3,072
WindowAttention (attn): 3-137	--	[1, 64, 1536]	[1, 64, 1536]	9,446,640	23,009,280

DropPath (drop path): 3-138	--	[1, 64, 1536]	[1, 64, 1536]	--	--
LayerNorm (norm2): 3-139	--	[1, 64, 1536]	[1, 64, 1536]	3,072	3,072
Mlp (mlp): 3-140	--	[1, 64, 1536]	[1, 64, 1536]	18,882,048	18,882,048
DropPath (drop path): 3-141	--	[1, 64, 1536]	[1, 64, 1536]	--	--
SwinBlock (23): 2-26	--	[1, 64, 1536]	[1, 64, 1536]	--	--
LayerNorm (norm1): 3-142	--	[1, 64, 1536]	[1, 64, 1536]	3,072	3,072
WindowAttention (attn): 3-143	--	[1, 64, 1536]	[1, 64, 1536]	9,446,640	23,009,280
DropPath (drop path): 3-144	--	[1, 64, 1536]	[1, 64, 1536]	--	--
LayerNorm (norm2): 3-145	--	[1, 64, 1536]	[1, 64, 1536]	3,072	3,072
Mlp (mlp): 3-146	--	[1, 64, 1536]	[1, 64, 1536]	18,882,048	18,882,048
DropPath (drop path): 3-147	--	[1, 64, 1536]	[1, 64, 1536]	--	--
LayerNorm (fc norm): 1-3	--	[1, 1536]	[1, 1536]	3,072	3,072
Linear (head): 1-4	--	[1, 1536]	[1, 8]	2,296	12,296